

Deformation Behavior and Damage-Induced Permeability Evolution of Sandy Mudstone Under Triaxial Stress

Yang Liu

Anhui University of Science and Technology

Tong Zhang (✉ 1099731996@qq.com)

Anhui University of Science and Technology

Yankun Ma

Anhui University of Science and Technology

Shuaibing Song

Anhui University of Science and Technology

Ming Tang

Anhui University of Science and Technology

Yanfang Li

Anhui University of Science and Technology

Research Article

Keywords: Sandy mudstone, Brittle-ductile transformation, Permeability evolution, Permeability model

Posted Date: January 3rd, 2022

DOI: <https://doi.org/10.21203/rs.3.rs-1119064/v1>

License: © ⓘ This work is licensed under a Creative Commons Attribution 4.0 International License.

[Read Full License](#)

Abstract

The permeability and mechanical behavior in sandy mudstone are crucial to the hazard prevention and safety mining. In this study, to investigate the evolution and characteristic of permeability and mechanical properties of mudstone during the in-site loading process, triaxial compression-seepage experiments were performed. The increase of permeability and decrease of mechanical strength gradually evaluated to the decrease of permeability and increase of mechanical strength subjected to the increase of confining stress from 5 to 15 MPa, which corresponds to the transformation from brittleness to ductility of mudstone, and the transformation threshold of 10 MPa confining stress was determined. The shear fractures across the sample at brittle regime, while shear fracture does not cross the sample or even be not generated at semibrittle and ductile state. The dynamic decrease, slight decrease, and residual response were determined in axial strain, and the divided zone increases with the increase of confining stress. The relatively higher permeability corresponds to the higher pore pressure as the increase of confining stress. The volumetric strain increases as the increase of confining stress, compared to that decrease correspond to the increase of the pore pressure, and the higher volumetric strain and the lower permeability. In addition, an improved permeability model was developed to describe the loading-based permeability behavior considering the Klinkenberg effect.

1 Introduction

The mechanical behaviors and seepage properties of sandy mudstone have been widely studied in the field of radioactive waste disposal, shale gas exploration, cap-rock behavior of hydrocarbon reservoirs, carbon geo-sequestration, underground coal gasification, and coal mining (Gale et al, 2007; Fu et al., 2015; Rezaeyan et al., 2015; Wilson et al., 2021). With increasing depth, the transitional deformation behavior from brittleness to ductility and complex transport characteristics occurred in the rock (Bishop, 1967; Renner et al., 2000; Nygård et al., 2006; Wu et al., 2021). At the macroscopic scale, brittle rock is characterized by a macroscopic fracture with much localized deformation, whereas ductile rock is distinguished by uniformly distributed deformation (Evans et al., 1990). Furthermore, the brittle-ductile transition deformation behavior can be obtained with a mixed microscopic transfiguration mechanism (Evans et al., 1990), while the permeability change varies with the mining activity. An abundant work focused on this field and outstanding findings were reported.

Existing studies in this area mainly focused on the destruction properties, which includes the bearing capacity and fracturing patterns (Petley, 1999; Renner et al., 2000; Boulin et al., 2013; Rezaeyan et al., 2015; Wu et al., 2021). Meanwhile, the stress depended brittle or ductile rock was also a hot issue, and it was evaluated using triaxial compression strengths and residual strengths (Rutter, 1986; Wang et al., 2019), as well as Young's modulus and Poisson's ratios during the linear elastic deformation stage (Rickman et al., 2008; Bai and Wierzbicki, 2010; Memon et al., 2020), of rocks under various stress situations. The two key parameters of internal friction angle and cohesion derived using the Mohr-Coulomb failure criterion may be used to define it for brittle rocks (Hucka and Das, 1974; Singh et al., 2011; Nooraiepour et al., 2017). The smaller disparity between the maximum strength and residual

strength, or the lower Young's modulus and internal friction angle of rocks, on the other hand, indicates a higher degree of ductility (Evans et al., 1990; Brantut et al., 2011; Wu et al., 2021).

The seepage property influences the mechanical behavior in mudstone. The permeability evolution of mudstone caused by different deformation modes, such as elastic deformation, brittle failure, and ductile deformation, is extensively investigated (Djeran-Maigre et al., 2000; Zhang and Rothfuchs, 2008; Zhang, 2016; Wu et al., 2021). The permeability is observed to drop fast during the early loading stage and later rise, and the permeability turning point associates well with the alteration in volumetric strain known as dilatancy (Schulze et al., 2001). Therefore, the permeability of mudstone in brittle regime increases considerably as dilatancy and failure develop, while the permeability of ductile mudstone keeps constant at the strain hardening stage (Popp et al., 2001; Alkan, 2009). Additionally, the dynamic response of permeability is reported by the pattern of localized or distributed deformation determined by the effective stress (De Paola et al., 2009). Wu et al., (2021) conducted a series of experiments, composed of the conventional triaxial compression tests, the hydrostatic loading-unloading tests, and the triaxial loading-unloading tests, on mudstone to study the permeability evolution at various stress conditions. Zhang et al., (2021) characterized the permeability variation of the fractured sandy mudstone by considering the impact of hydro-mechanical coupling, fracture morphology, and mineral composition. In addition, the permeability models are usually developed on different empirical functions, such as exponential functions (Seidle et al., 1992; Li et al., 2013; Tan et al., 2019), cubic functions (Gangi, 1978; Kwon et al., 2001) and logarithmic functions (Kranzz et al., 1979; Walsh, 1981). To predict the coal permeability at the yielding and post-failure stage, Xue et al., (2015) developed a permeability model considering the damage process. To define the variation in coal permeability when effective stress changes from the elastic deformation stage to the post-peak stage, Chen et al. (2016) introduced an effective stress-dependent exponential permeability model. To investigate the permeability behavior with stress varies throughout the unloading process, Zhang et al., (2017) put forward an analytical permeability model that included the influence of damage evolution.

The change in mudstone permeability and mechanical properties caused by mining activity is complex, it would be of great significance to investigate the mechanical behavior and transport properties of mudstone subjected to the in-site stress impact. In this study, the triaxial compression-seepage experiments were performed, and the relationship of damage behavior and seepage characteristics and the influence of deformation on permeability response at brittle or ductile state were analyzed. An improved permeability model was developed, and the permeability evolution of mudstone was discussed.

2 Experimental Section

2.1 Sample preparation

The dark grayish sandy mudstone block used in this study was collected from a coal mine in the Ordos Basin, which has bedding and clastic texture, showing foliated fabric described by light and dark bands. Some cylindrical samples, with a diameter of 50 mm, were drilled parallel to the bedding planes of the

sandy mudstone block by a core-drilling machine. Then the cylinders were shaped to $\phi 50 \times 100$ mm cylindrical samples by a grinding device with a high-precision standard. The X-ray diffraction (XRD) results show that the sandy mudstone mainly consists of clay mineral (24.3%), quartz (20.7%), plagioclase (15%), ankerite (15%), calcite (11.3%), and other minerals (13.7%). The averaged density and porosity of the sandy mudstone are 1.99 g/cm^3 and 8.1%, respectively.

2.2 Experimental apparatus

The triaxial seepage tests were conducted using a hydromechanical coupling triaxial permeation apparatus (Fig. 1). A servo-hydraulic double pump booster was utilized to control the confining pressure up to 70 MPa with an accuracy of 0.01 MPa, and a servo-hydraulic booster was applied to ensure the axial force up to the maximum force of 1000 kN. A gas pressure reducing valve and two different gas mass flow controllers were employed to regulate the gas pressure and flow. The axial strain and the radial strain were measured by a linear variable differential transducer (LVDT) and an extensometer chain, respectively. The apparatus can provide an axial and confining stress acting on the samples with a stable temperature during measuring permeability in this work.

2.3 Experimental procedure

In this work, N_2 with a purity of 99.999% was chosen as the testing gas, and different confining stresses (5 MPa, 10 MPa, and 15 MPa) and gas pressures (2 MPa, 3 MPa, and 4 MPa) were considered in the experimental tests. Nine sandy mudstone samples were prepared, and each test corresponded to one sample under one stress state. Axial stress was applied at a rate of 0.1 mm/min using a displacement control, and all the experimental tests were carried out at 25°C . Moreover, the sample information and experimental conditions used in each test were listed in Table 1. The specific test procedure is described below: (1) The sandy mudstone samples were firstly dried at a constant temperature of 50°C for 48 h. And then the dried sandy mudstone sample was sealed with the base pedestal and top cap by the heat shrinkable sleeve. Subsequently, the sample was placed into the triaxial pressure cell. (2) After completing the installation of the triaxial cell, the air compressor was opened to discharge air and fill the triaxial cell with silicone oil. And then the axial stress and confining stress were set to predefined values. (3) Afterwards, the outlet valve was closed and the vacuum pump was turned on to vacuum degassing the sample for 2h. And then N_2 with specified pressure was injected to the lower end of the sample and finally flowed to the outlet via a stainless steel pipe which is connected to the gas mass flow controller. Finally, the axial stress controlled by displacement control mode was loaded to the higher end of the sample until destruction.

Table 1
Information of rock samples

Specimen No.	D (mm)	L (mm)	ρ (g/cm ³)	σ_3 (MPa)	P_1 (MPa)
S1	49.45	100.18	1.98	5	2
S2	50.04	99.95	2.05	5	3
S3	50.23	100.16	1.96	5	4
S4	50.03	100.20	1.97	10	2
S5	49.36	100.21	2.05	10	3
S6	49.62	100.28	1.95	10	4
S7	49.48	100.07	2.03	15	2
S8	50.07	99.81	1.98	15	3
S9	50.04	100.16	1.97	15	4
Note: D - Diameter; L - Length; ρ - Averaged Density; σ_3 - Confining Pressure; P_1 - inlet gas Pressure;					

Considering Darcy's law, the permeability of sandy mudstone was obtained:

$$k = \frac{2qP_0\mu L}{A(P_1^2 - P_2^2)}$$

1

where k is the permeability (m²); q is the gas permeation rate (m³/s); P_0 is the standard atmospheric pressure (Pa); μ is the gas kinematic viscosity (Pa·s); L is the length of the rock sample (m); A is the cross-sectional area of the rock sample (m²); P_1 is the inlet or upper stream gas pressure (Pa); P_2 is the outlet or downstream gas pressure (Pa).

3 Results And Discussion

3.1 Mechanical behavior and permeability evolution

The bearing capacity and transport property of rock are prominently determined by its mineral grains composition and pore-fracture system. With the change of stress condition, the response of deformation and permeability behavior keeps a dynamic process. The pore-fracture structure and texture of rock are the main reasons for the difference in initial permeability. The deformation behavior, both of brittle and ductile rock, can be divided into five typical stages (Fig. 2), and the most difference between brittle and ductile rock is at the fifth stage, termed strain softening stage and strain hardening stage, respectively.

Correspondingly, this distinction is related to different deformation mechanisms, further leading to the variable permeability behaviors.

3.1.1 The impact of confining stress

The relationships of stress-strain-permeability of sandy mudstone are shown in Fig. 3 and the volumetric strain-axial strain behaviors are shown in Fig. 4. The sandy mudstone performs brittle, brittle-ductile transition, and ductile under the studied confining stresses. The deformation behavior of sandy mudstone characterized brittle deformation under a low confining pressure of 5 MPa, and its deformation behavior consists of five classical stages: the compaction stage (I), the elastic deformation stage (II), the yielding stage (III and IV), and the post-destruction stage (V) (Fig. 3a-c), which leads to different corresponding permeability evolution (Fig. 2a). At the beginning of Stage I, the total volume and permeability decrease fastly with the deviatoric stress increasing due to the pre-existing microcracks closed continuously. Once reach Stage II, only restricted microcracks generate so the permeability decreases slowly without increase. And the elastic modulus can be altered as primary cracks close continuously in this stage. In Stage III and IV, the fractures start to grow and coalesce to each other, while the permeability did not increase, but continued to decrease gradually which presumably because the macro-fracture is not formed and the cracks are still compressed. In these stages, it leads to plastic strain which is followed by a volume increase (Fig. 4a) or dilatancy (Fig. 4b and c) due to microfracturing, and reduced bearing capacity and elastic modulus of sandy mudstone. In Stage V, the macroscopic fracture which cut through the end of specimen formed by the coalescence of grain boundary and intragranular cracks, resulting in the permeability behavior of sudden increase and then a gradual increase (Paterson and Wong, 2005). After the sample failure, the permeability normally remains constant or slightly undulates, which is presumably because of the constriction and blocking by dislodging particles of the formerly established gas flow paths (Hangx et al., 2010). Furthermore, as shown in Fig. 3a-c, the permeability evolution after the sample failure does not increase a lot, and the incremental permeability is even lower than the original permeability for sandy mudstone.

Under higher confining pressure of 10-15 MPa, the deformation behavior of sandy mudstone showed brittle-ductile transition and ductile deformation characteristics, and its deformation characteristic is also composed of five stages (Fig. 2b). In Stage I and II, the permeability decreases because the pre-existing microcracks closed continuously, which is similar to brittle deformation characteristics. Despite the presence of microcracks in Stage III and IV, the fractures are prevented and the dislocation mobility is enhanced. Hence, the permeability gradually decreases. Note that the volumetric strain curve of brittle-ductile transition sandy mudstone approximatively keeps symmetric parabola distribution characteristics before the dilatancy stage (Fig. 4d-f). In Stage V, with the deviatoric stress increasing, the shear bands generate, nucleate and develop to form a shear macro-fracture at a high angle with the compacted stress for brittle-ductile transition sandy mudstone and it does not penetrate the two end surfaces. For ductile sandy mudstone, strain localization can occur, involving mainly cracking, in which case the rock accumulates distributed microcracks without any macroscopic rupture. Therefore, the brittle-ductile and ductile deformation of sandy mudstone at normal temperature is mainly attributed to the plastic flow

deformation mechanism. Different from brittle sandy mudstone, the permeability of brittle-ductile transition sandy mudstone keeps stabilized or decreases a little as the high-angle shear fractures. In contrast to the ultimate permeability evolution of damaged brittle-ductile transition sandy mudstone, the permeability of ductile sandy mudstone has a slightly reduced trend at the strain hardening process because of the cataclastic flow behavior. In general, the permeability decreases as an exponential pattern under the whole compaction process for both brittle-ductile transition and ductile sandy mudstone.

The comparison of stress-strain and permeability-strain behavior of sandy mudstone under different confining pressures is presented in Fig. 5. As shown in Fig. 6, when the confining pressure is small, the rock is brittle and prone to shear failure. With the confining pressure increasing, the test results gradually show the characteristics of weakening brittleness, increasing ductility and transformation from brittleness to ductility. In this study, as the gas pressure is constant, the sandy mudstones transform from strain softening at the post-peak stage to strain hardening state with confining pressure increasing (Fig. 5). In light of Cao et al., (2005) and Yu et al., (2013), the confining pressure threshold of brittle-ductile transition critical state is finally determined as 10MPa for studied sandy mudstone.

3.1.2 The impact of pore pressure

The comparison of stress-strain and permeability-strain behavior of sandy mudstone under different gas pressures is shown in Fig. 7. When the confining pressure is small and constant ($\sigma_3 = 5$ MPa), the deformation and permeability evolution were similar and the increased permeability of sample S1, S2, and S3 at the destruction stage are 2.89, 3.12, and 4.63% with the increase of pore pressure, respectively, indicating that enlarging the gas pressure can increase the seepage channel at the post-peak stage. Different from the brittle sandy mudstone, the permeability of both brittle-ductile transition and ductile sandy mudstone at Stage V maintains constant or decreases a little, mainly because they did not develop shear fracture penetrating the top and bottom surfaces, even the pore pressure is increased to reduce the effective stress. Overall, the alteration of gas pressure has little effect on sandy mudstone with different deformation regimes.

3.2 Failure modes of sandy mudstone

The failure characteristics of sandy mudstone are presented in Fig. 8, and the corresponding SEM results are shown in Fig. 9. The samples S1, S2, and S3 (brittle sandy mudstone) formed intuitionistic macroscopic shear fractures without cohesion after destruction. The semibrittle sandy mudstone (at brittle-ductile transition) developed a high-angle shear macro-fracture with a few cohesive and it does not pierce the top and bottom end surfaces, while the ductile sandy mudstone showed fully plastic flow deformation, which undergoes homogeneous large strains without macrofracturing. At the microscopic scale, the brittle regimes of sandy mudstone are mainly composed of cataclastic flow, which involves cracking (either intragranular or intergranular), and is distinctly different from the initial state. There is a mixed behavior (cataclastic and plastic flow) that can be observed for brittle-ductile transition sandy mudstone in Fig. 9c. Comparing the microscopic observation of brittle sandy mudstone, the micro-processes of ductile sandy mudstone can be fully plastic with elevated confining pressure.

4 Improved Permeability Model

4.1 Model development

As the internal microstructure of sandy mudstone consists of cracks and matrices, the sandy mudstone can be presumed to be the matchstick geometry. As a result, the classical exponential permeability model for sandy mudstone at elastic state can be presented as (Seidle et al., 1992):

$$k_i = k_0 e^{-3C_f(\sigma_e - \sigma_{e0})}$$

2

where k_i is the permeability of sandy mudstone, m^2 ; k_0 is the initial permeability of sandy mudstone, m^2 ; C_f is the compression coefficient of fractures, MPa^{-1} ; σ_e is the effective stress, MPa ; and the σ_{e0} is the initial effective stress, MPa .

Klinkenberg (1941) pointed that the gas slippage phenomenon will be significant as the flow path size in fracture closes to the mean free path of the gas molecules at a lower gas pressure, which will further affect the permeability. So, by considering the Klinkenberg effect, the exponential permeability equation can be represented as:

$$k_i = k_{ini} \left(1 + \frac{B}{P} \right) e^{-3C_f(\sigma_e - \sigma_{e0})}$$

3

where B is the Klinkenberg constant, MPa ; P is the mean pore pressure, MPa .

In this study, the Boit's coefficient is considered to remain constant at 1, and the effective stress in deviatoric stress loading can be expressed as (Chen et al., 2016):

$$\sigma_e = \frac{3P_{eff} + \Delta\sigma}{3}$$

4

where P_{eff} is the effective confining stress which equals to the confining stress σ_3 minus the pore pressure P , MPa ; $\Delta\sigma$ is the deviatoric stress, MPa .

According to the experimental results, the permeability decreases continuously in the yielding stage, and it remains unchanged or slightly decreases at strain hardening process for ductile and brittle-ductile transition sandy mudstone with increasing of the effective stress, so the exponential permeability model (Eq. 3) can depict the variation process of permeability well in all stages. However, for brittle and some semibrittle sandy mudstone, the permeability shows a large increase with the decrease of effective stress

in the post-peak stage. Hence, the exponential permeability model could not describe the change process of permeability in the post-peak stages for brittle and some semibrittle sandy mudstone.

To better describe permeability behavior under the overall triaxial compression process for brittle and some semibrittle sandy mudstone, a correction factor β is imported to enhance the prediction accuracy of permeability. The correction factor β can be introduced as the modified coefficient for the difference between the predicted permeability and the test permeability, corresponding to the effective stress. Furthermore, the peak point of the effective stress is regarded as a distinguishing point for brittle and some semibrittle sandy mudstone due to the permeability before and after failure varies dramatically, which is defined as σ_s . Based on the thinking of symmetry, the improved piecewise permeability model before and after σ_s , combining the correction factor β , can be updated as:

$$\begin{cases} k_i = k_{ini} \left(1 + \frac{B}{P} \right) e^{-3C_f(\sigma_e - \sigma_{e0})}, \sigma_e \leq \sigma_s \\ k_i = \beta(\sigma_e) k_{ini} \left(1 + \frac{B}{P} \right) e^{-3C_f(2\sigma_s - \sigma_e - \sigma_{e0})}, 2\sigma_s - \sigma_e > \sigma_s \end{cases} \quad (5)$$

The relationship between the correction factor β and the deviatoric effective stress can be acquired using Eq. 3 and experimental permeability data. Then, the correction function of β can be obtained by fitting the results. Fig. 10 illustrates the relationship between the modification factor β and the effective stress after symmetry for studied brittle and some semibrittle sandy mudstone. And the correction function of β can be gained by fitting, which is expressed as Eq. 6.

$$\beta = a(2\sigma_s - \sigma_e) + b$$

6

where a and b are the fitting parameters, and the analogous results of fitting parameters are used at the residual stress stage.

4.2 Model validation

To verify the revised permeability model, the analytical permeabilities acquired using Eqs. 3, 5, and 6 are compared with the test results for the sandy mudstone in triaxial compression tests (see Fig. 11). And the corresponding parameters applied in the improved models are summarized in Tables 2 and 3.

Table 2
Parameters of the improved permeability models

Specimen No.	k_{ini}	B	C_f
S1	7.430	0.025	0.019
S2	1.3145	0.298	0.010
S3	13.473	0.039	0.017
S4	2.595	0.041	0.014
S5	15.011	0.084	0.017
S6	7.681	0.098	0.017
S7	5.087	0.061	0.015
S8	6.352	0.157	0.021
S9	7.739	0.320	0.016

Table 3
Parameters used in the modified function of β

Specimen No.	a		b	
	Fitting value	Mean value	Fitting value	Mean value
S1	0.079	0.059	0.130	0.293
S2	0.042		0.569	
S3	0.074		0.457	
S5	0.046		0.205	
S6	0.054		0.106	

As listed in Table 3, the fitted parameter a for correction factor β is in range of 0.042 – 0.079 with a mean value of 0.059, and the fitted parameter b is in the range of 0.106 – 0.569 with a mean value of 0.293, indicating that the average relative errors between the experimental data and model prediction for sandy mudstone decreases linearly as the effective stress decrease at residual stress stage, and can be estimated by $0.059(2\sigma_e - \sigma_s) + 0.293$. As shown in Fig. 11, the permeability increases slightly with the effective stress further decreasing at the residual stress stage for brittle sandy mudstone (Fig. 11a-c). Figure 11d and e presents that the permeability keeps constant or decreases a little after peak effective stress for brittle-ductile transition sandy mudstone. For ductile sandy mudstone, the permeability decreases continuously with the effective stress increases (Fig. 11g-i). For brittle and semibrittle sandy mudstone, the results can be modeled well, except Sample S2 (Fig. 11b), using Eqs. 5 and 6. The results of sample S4 after peak effective stress are not modeled because Sample S4 does not reach the residual stress stage. Equation 3 is used for ductile sandy mudstone in triaxial compression tests, and it matches

well between the experimental data and model (Fig. 11g-i). Notably, the mentioned permeability model focus on characterizing the permeability evolution of different deformation regime of sandy mudstone with the effective stress varies from elastic deformation to failure, and some empirical parameters are used in the model. Therefore, this model is an exploration for clay rock and necessitates further validation and improvement for better presentation and broader applications in future studies.

5 Conclusions

In this study, a series of triaxial compression-seepage experiments were conducted on sandy mudstone, and the response of permeability and mechanical properties was observed. To describe the permeability behavior in the whole process of triaxial compression, an improved permeability model of sandy mudstone considering the Klinkenberg effect was proposed. The main findings are as follows:

(1) The confining pressure has more contribution to the brittle-ductile transformation than pore pressure for sandy mudstone. As the increase of confining stress, increasing ductility and transformation from brittleness to ductility was observed, and the brittle and ductile state in sandy mudstone was determined. The permeability of the mudstone gradually decreases in the ductile stage. The permeability does not increase a lot and the final permeability is even lower than the initial permeability at brittle state, while the permeability usually keeps constant or decreases a little for brittle-ductile transition and ductile sandy mudstone.

(2) The failure modes corresponding to the brittle and ductile state are different. A macroscopic shear fracture generated after destruction for brittle sandy mudstone crosses the ends of the sample with the microscopic observation of cataclastic flow, while the developed high-angle shear band is not across at semibrittle state, which has a mixed behavior (cataclastic and plastic flow) at the microscopic scale. For ductile state, it usually undergoes homogeneous large strains without macrofracturing and can be fully plastic flow at strain hardening stage.

(3) The improved permeability model is developed based on the classical exponential permeability model and slippage effects. The correction factor β related linearly to the effective stress can well reflect the difference between the measured permeability and the permeability obtained from the improved model. And the damage-based permeability was well described.

Declarations

Acknowledgements

This paper was supported by the National Youth Science Foundation (nos.51904011), Anhui Provincial Natural Science Foundation (nos.1908085QE183), Anhui University Scientific Research Foundation (no.QN2018108), the Open Fund of State Key Laboratory of Water Resource Protection and Utilization in Coal Mining (Grant No.GJNY-18-73.7), the Institute of Energy, Hefei Comprehensive National Science Center under Grant No.21KZS216.

Ethical Statement

We certify that this manuscript is original and has not been published and will not be submitted elsewhere for publication while being considered by Natural Hazards. And the study is not split up into several parts to increase the quantity of submissions and submitted to various journals or to one journal over time. No data have been fabricated or manipulated (including images) to support your conclusions. No data, text, or theories by others are presented as if they were our own. The submission has been received explicitly from all co-authors. And authors whose names appear on the submission have contributed sufficiently to the scientific work and therefore share collective responsibility and accountability for the results.

Conflict of interest

The authors declare no conflict of interest.

CRediT authorship contribution statement

Yang Liu: Conceptualization, Formal analysis, Investigation, Data curation, Writing – original draft. **Tong Zhang:** Conceptualization, Writing – review & editing, Funding acquisition, Supervision. **Yankun Ma:** Conceptualization, Supervision. **Shuaibing Song:** Writing – review & editing. **Ming Tang:** Visualization. **Yanfang Li:** Visualization.

Author contributions sections

The manuscript was written through the contributions of all authors. All authors have given approval to the final version of the modified manuscript.

References

1. Alkan H, Cinar Y, Pusch G (2007) Rock salt dilatancy boundary from combined acoustic emission and triaxial compression tests. *International Journal of Rock Mechanics and Mining Science* 44(1):108–119
2. Alkan H (2009) Percolation model for dilatancy-induced permeability of the excavation damaged zone in rock salt. *International Journal of Rock Mechanics and Mining Science* 46(4):716–724
3. Bai Y, Wierzbicki T (2010) Application of extended Mohr-Coulomb criterion to ductile fracture. *Int J Fract* 161(1):1–20
4. Bishop AW (1967) Progressive failure with special reference to the mechanism causing it. *Proceedings of the Geotechnical Conference Oslo 2*, 142–150
5. Boulin PF, Bretonnier P, Vassil V, Samouillet A, Fleury M, Lombard JM (2013) Sealing efficiency of caprocks, experimental investigation of entry pressure measurement methods. *Mar Pet Geol* 48:20–30

6. Brantut N, Schubnel A, Guéguen Y (2011) Damage and rupture dynamics at the brittle-ductile transition, the case of gypsum. *Journal of Geophysical Research, Solid Earth* 116:B01404
7. Cao WG, Wang HH, Zhang S, He W (2005) Study on decision of conversion condition for brittle-ductile property of rock by statistical damage method. *Chinese Journal of Geotechnical Engineering* 27(12):1391–1396
8. Chen D, Pan Z, Shi JQ, Si G, Ye Z, Zhang J (2016) A novel approach for modelling coal permeability during transition from elastic to post-failure state using a modified logistic growth function. *Int J Coal Geol* 163:132–139
9. De Paola N, Faulkner DR, Collettini C (2009) Brittle versus ductile deformation as the main control on the transport properties of low-porosity anhydrite rocks. *Journal of Geophysical Research: Solid Earth* 114:B06211
10. Djeran-Maigre I, Gasc-Barbier M (2000) Hydromechanical modelling of experimentally compacted saturated argillaceous porous Media. *Transp Porous Media* 41:81–103
11. Evans B, Fredrich JT, Wong TF (1990) The brittle-ductile transition in rocks, recent experimental and theoretical progress. *The Brittle-Ductile Transition in Rocks, Geophysical Monograph* 56:1–20
12. Fu X, Jia R, Wang H, Wu T, Meng L, Sun Y (2015) Quantitative evaluation of fault-caprock sealing capacity, a case from Dabei-Kelasu structural belt in Kuqa Depression, Tarim Basin, NW China. *Pet Explor Dev* 42(3):329–338
13. Gangi AF (1978) Variation of whole and fractured porous rock permeability with confining pressure. *International Journal of Rock Mechanics and Mining Science & Geomechanics Abstracts* 15(5):249–257
14. Gale JFW, Reed RM, Holder J (2007) Natural fractures in the Barnett shale and their importance for hydraulic fracture treatment. *AAPG Bull* 91(4):603–622
15. Hangx SJT, Spiers CJ, Peach CJ (2010) The effect of deformation on permeability development in anhydrite and implications for caprock integrity during geological storage of CO₂. *Geofluids* 10(3):369–387
16. Hucka V, Das B (1974) Brittleness determination of rocks by different methods. *International Journal of Rock Mechanics and Mining Science & Geomechanics Abstracts* 11(10):389–392
17. Klinkenberg LJ (1941) The permeability of porous media to liquids and gases. *API Drilling and Production Practice* 2(2):200–213
18. Kranzz RL, Frankel AD, Engelder T, Scholz CH (1979) The permeability of whole and jointed Barre granite. *International Journal of Rock Mechanics and Mining Science & Geomechanics Abstracts* 16(4):225–234
19. Kwon O, Kronenber AK, Gangi AF, Johnson B (2001) Permeability of Wilcox shale and its effective stress law. *Journal of Geophysical Research, Solid Earth* 106(B9):19339–19353
20. Li S, Tang D, Pan Z, Xu H, Huang W (2013) Characterization of the stress sensitivity of pores for different rank coals by nuclear magnetic resonance. *Fuel* 111:746–754

21. Martin CD, Chandler NA (1994) The progressive fracture of Lac du Bonnet granite. *International Journal of Rock Mechanics and Mining Science & Geomechanics Abstracts* 31(6):643–659
22. Memon KR, Mahesar AA, Ali M, Tunio AH, Mohanty US, Akhondzadeh H, Awan FU, Iglauer S, Keshavarz A (2020) Influence of cryogenic liquid nitrogen on petro-physical characteristics of mancos shale, an experimental investigation. *Energy Fuels* 34(2):2160–2168
23. Nooraiepour M, Haile BG, Hellevang H (2017) Compaction and mechanical strength of Middle Miocene mudstones in the Norwegian North Sea-The major seal for the Skade CO₂ storage reservoir. *Int J Greenhouse Gas Control* 67:49–59
24. Nygård R, Gutierrez M, Bratli RK, Høeg K (2006) Brittle-ductile transition, shear failure and leakage in shales and mudrocks. *Mar Pet Geol* 23(2):201–212
25. Paterson MS, Wong TF (2005) *Experimental Rock Deformation-The Brittle Field*. Springer Science & Business Media
26. Petley DN (1999) Failure envelopes of mudrocks at high confining pressures. *Geological Society of London Special Publications* 158(1):61–71
27. Popp T, Kern H, Schulze O (2001) Evolution of dilatancy and permeability in rock salt during hydrostatic compaction and triaxial deformation. *Journal of Geophysical Research: Solid Earth* 106(B3):4061–4078
28. Renner J, Hettkamp T, Rummel F (2000) Rock mechanical characterization of an argillaceous host rock of a potential radioactive waste repository. *Rock Mech Rock Eng* 33(3):153–178
29. Rezaeyan A, Tabatabaei-Nejad SA, Khodapanah E, Kamari M (2015) A laboratory study on capillary sealing efficiency of Iranian shale and anhydrite caprocks. *Mar Pet Geol* 66:817–828
30. Rickman R, Mullen MJ, Petre JE, Grieser WV, Kundert D (2008) A practical use of shale petrophysics for stimulation design optimization: all shale plays are not clones of the Barnett Shale. *SPE Annual Technical Conference and Exhibition*
31. Rutter EH (1986) On the nomenclature of mode of failure transitions in rocks. *Tectonophysics* 122(3–4):381–387
32. Schulze O, Popp T, Kern H (2001) Development of damage and permeability in deforming rock salt. *Eng Geol* 61(2–3):163–180
33. Seidle JP, Jeansonne MW, Erickson DJ (1992) Application of matchstick geometry to stress dependent permeability in coals. *SPE Rocky Mountain Regional Meeting, Casper, Wyoming*, SPE-24361-MS
34. Singh M, Raj A, Singh B (2011) Modified Mohr-Coulomb criterion for non-linear triaxial and polyaxial strength of intact rocks. *Int J Rock Mech Min Sci* 48(4):546–555
35. Tan Y, Pan Z, Feng XT, Zhang D, Connell LD, Li S (2019) Laboratory characterisation of fracture compressibility for coal and shale gas reservoir rocks, a review. *Int J Coal Geol* 204:1–17
36. Walsh JB (1981) Effect of pore pressure and confining pressure on fracture permeability. *International Journal of Rock Mechanics and Mining Science & Geomechanics Abstracts* 18(5):429–

37. Wang H, Wu T, Fu X, Liu B, Wang S, Jia R, Zhang C (2019) Quantitative determination of the brittle-ductile transition characteristics of caprocks and its geological significance in the Kuqa depression, Tarim Basin, western China. *Journal of Petroleum Science and Engineering* 173:492–500
38. Wilson J, Bateman K, Tachi Y (2021) The impact of cement on argillaceous rocks in radioactive waste disposal systems, A review focusing on key processes and remaining issues. *Appl Geochem* 130:104979
39. Wu T, Fu X, Liu B, Wang H, Xie Z, Zhejun, Pan (2021) Mechanical behavior and damage-induced permeability evolution of mudstone and gypsum caprocks. *J Petrol Sci Eng* 196:108079
40. Xue Y, Gao F, Liu X (2015) Effect of damage evolution of coal on permeability variation and analysis of gas outburst hazard with coal mining. *Nature Hazards* 79(2):999–1013
41. Yu J, Li H, Chen X, Chai YY, Wu N, Mu K (2013) Triaxial experimental study of associated permeability-deformation of sandstone under hydro-mechanical coupling. *Chinese Journal of Geotechnical Engineering* 32(6):1203–1213
42. Zhang CL, Rothfuchs T (2008) Damage and sealing of clay rocks detected by measurements of gas permeability. *Physical and Chemistry of the Earth Parts A/B/C* 33:S363–S373
43. Zhang CL (2016) The stress-strain-permeability behaviour of clay rock during damage and recompaction. *J Rock Mech Geotech Eng* 8(1):16–26
44. Zhang XM, Zhang DM, Leo CJ, Yin GZ, Feng D, Liyanapathirana DS (2017) Damage evolution and post-peak gas permeability of raw coal under loading and unloading conditions. *Transport Porous Media* 117(3):465–480
45. Zhang T, He X, Liu Y, Zhao Y, Yu X (2021) Experimental study on permeability response in fractured rock to the effect of hydro-mechanical coupling, fracture geometry, and component content. *Nature Hazards* 105:1439–1451

Figures

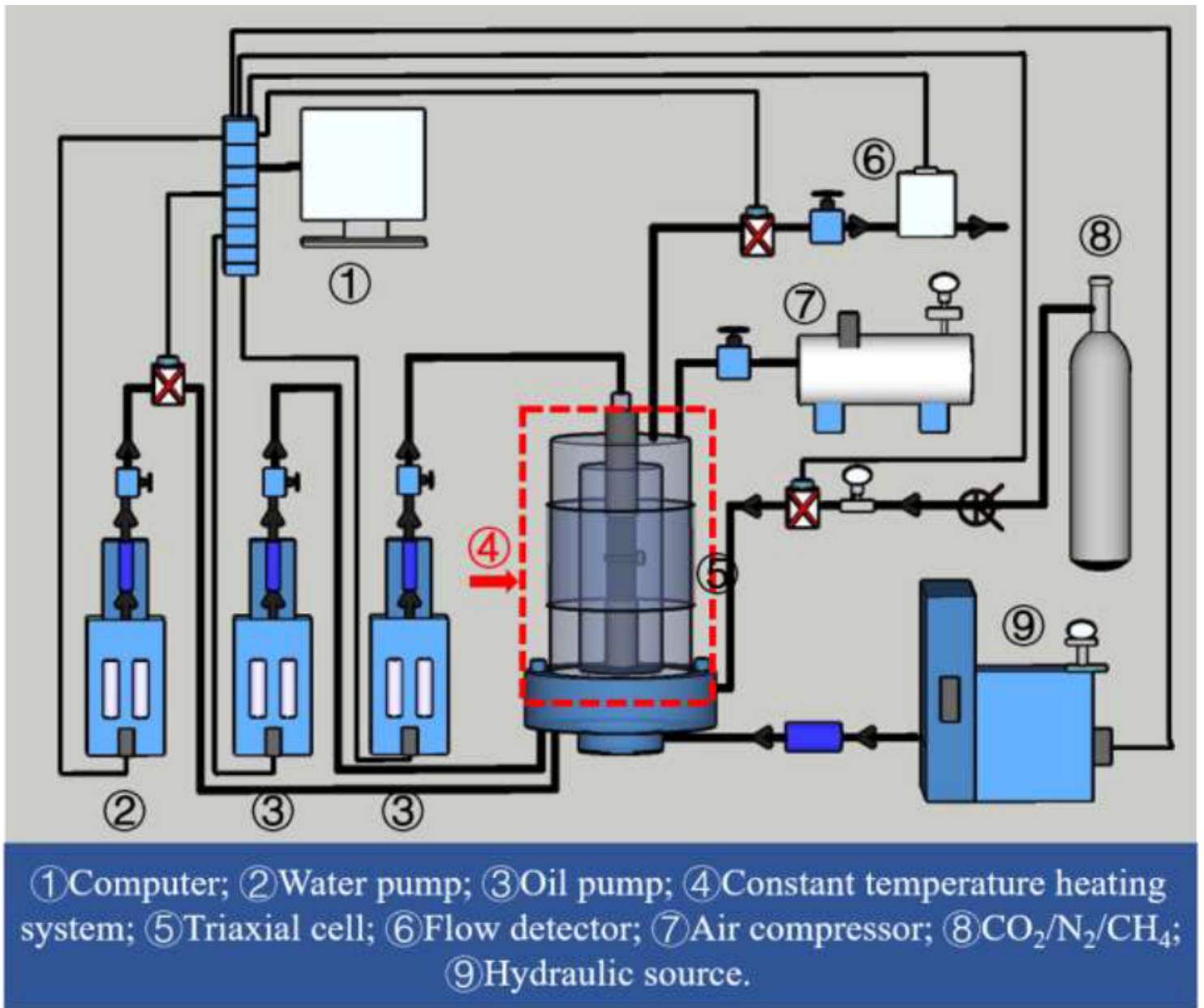


Figure 1

Triaxial mechanical-seepage coupling experimental apparatus.

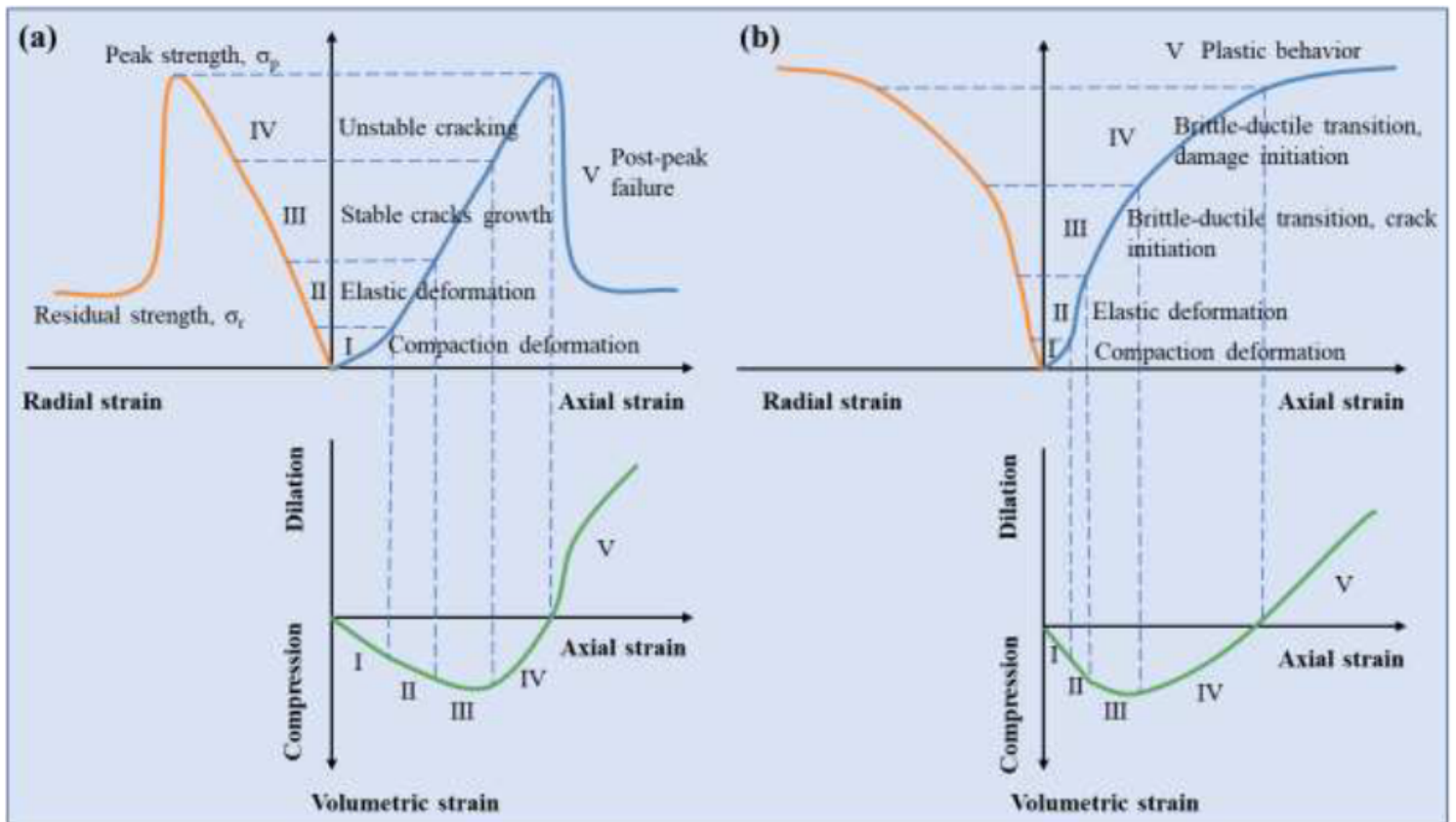


Figure 2

The diagram of the typical deviatoric stress-strain and volumetric strain-axial strain curves of brittle rocks (a) and ductile rocks (b) under triaxial compression tests [1,22].

Figure 3

Relationship for stress-strain-permeability of sandy mudstone in triaxial compression and permeability tests.

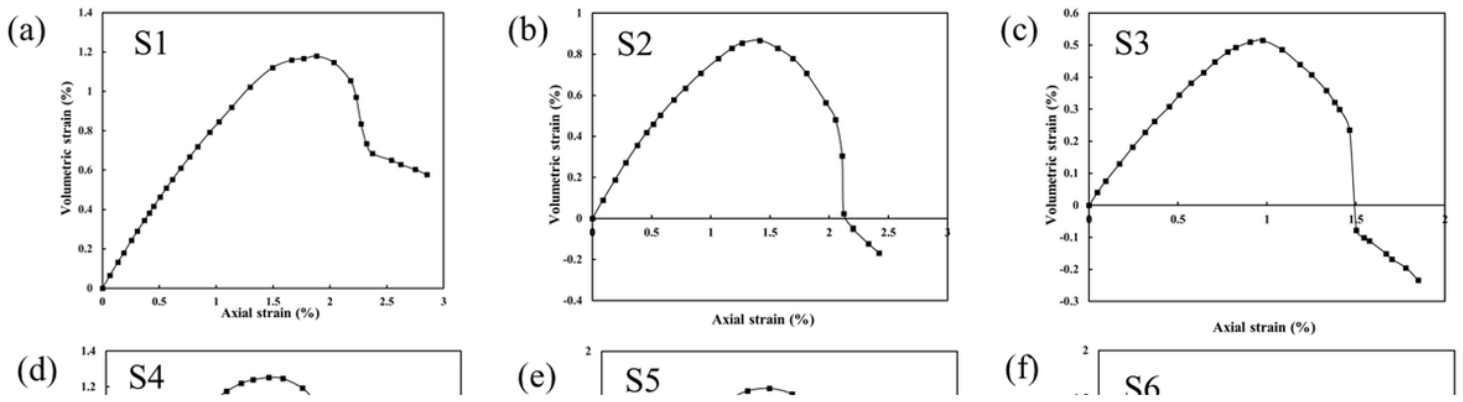


Figure 4

Relationship for volumetric strain and axial strain of sandy mudstone in triaxial compression and permeability tests

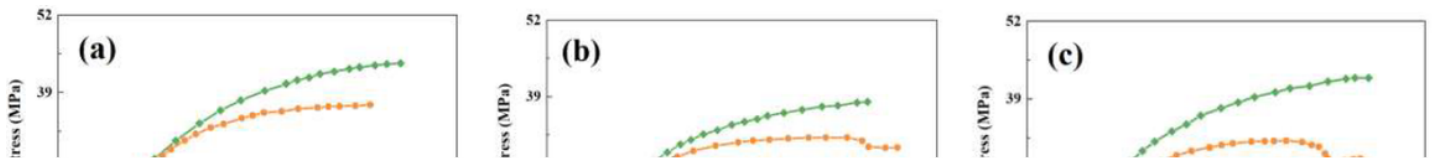


Figure 5

The differential stress, permeability and volumetric strain data are plotted versus axial strain for sandy mudstone in different gas pressures triaxial compression and permeability tests (a-c is gas pressure of 2 MPa, 3 MPa and 4 MPa, respectively).

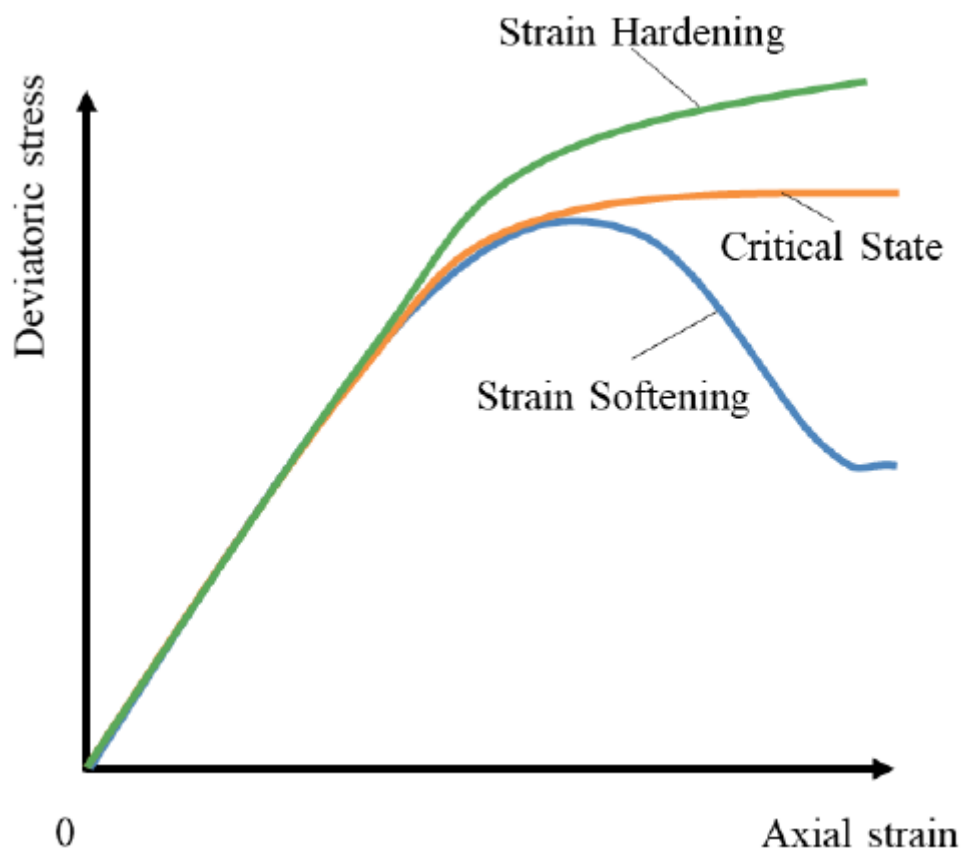


Figure 6

The diagram of brittle-ductile transition curves of rock [7].

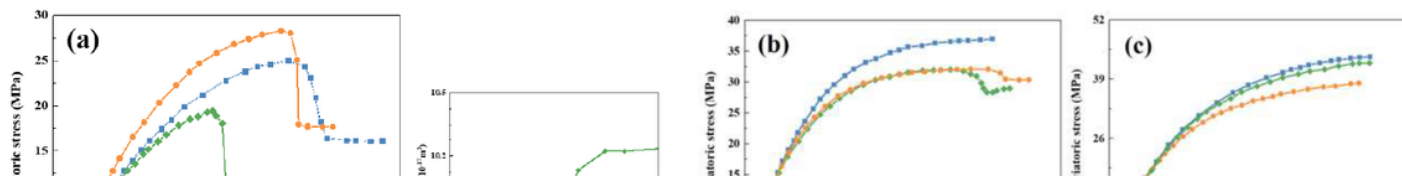


Figure 7

The differential stress, permeability and volumetric strain data are plotted versus axial strain for sandy mudstone in different confining pressures triaxial compression and permeability tests (a-c is confining pressure of 5 MPa, 10 MPa and 15 MPa, respectively).

Figure 8

The failure characteristics of sandy mudstone in triaxial compression and permeability tests.

Figure 9

SEM pictures of sandy mudstone at (a) initial state, (b) brittle failure state, (c) brittle- ductile transition and (d) ductile failure state.

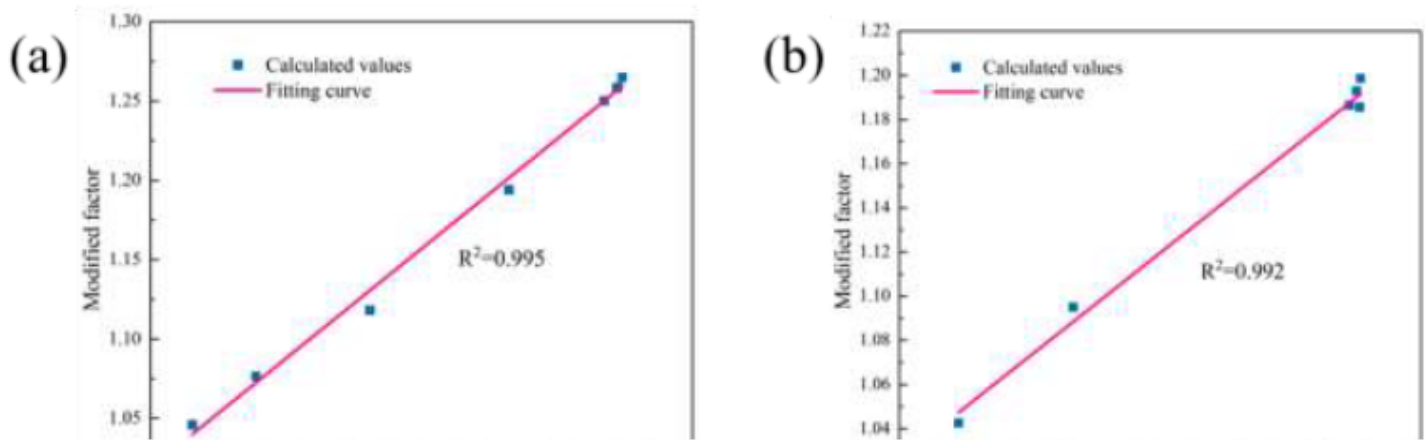


Figure 10

Relationship between modified factor and effective stress after symmetry at $\sigma_e = \sigma_s$ for (a) Sample S1, (b) Sample S2, (c) Sample S3, (d) Sample S5 and (e) Sample S6.

Figure 11

Permeability of sandy mudstone in triaxial compression tests, and modeling results from the improved model i.e., Eqs. (3), (5) and (6).